Journal of Geophysical Research: Solid Earth

RESEARCH ARTICLE
10.1029/2018JB015638

Smoothing of Fault Slip Surfaces by Scale-Invariant Wear

Kelian Dascher-Cousineau[1], **James D. Kirkpatrick**[1], **and Michele L. Cooke**[2]

[1]Department of Earth and Planetary Sciences, McGill University, Montreal, Quebec, Canada, [2]University of Massachusetts Amherst, MA, USA

Key Points:
- Fault slip surfaces smooth with slip
- Wear on fault slip surfaces is scale invariant
- Multiscale asperity failure is the predominant wear mechanism

Supporting Information:
- Supporting Information S1

Correspondence to:
K. Dascher-Cousineau,
kdascher@ucsc.edu

Citation:
Dascher-Cousineau, K., Kirkpatrick, J. D., & Cooke, M. L. (2018). Smoothing of fault slip surfaces by scale-invariant wear. *Journal of Geophysical Research: Solid Earth*, *123*, 7913-7930. https://doi.org/10.1029/2018JB015638

Received 14 FEB 2018
Accepted 28 AUG 2018
Accepted article online 3 SEP 2018
Published online 24 SEP 2018

Abstract Previous field observations suggest that fault slip surface roughness may decrease with slip. However, measurements have yet to confidently isolate the effect of slip from other possible controls, such as lithology or tectonic setting. We describe the evolution of slip surfaces in normal faults in SE Utah that cut well-sorted, high-porosity sandstones and accommodated regional extension at 1- to 4-km depth. Tight controls on fault offset and uniform tectonic history allowed us to isolate the effect of slip during early stages of faulting (0- to 55-m slip). Slip surfaces progress from rough joints and deformation bands toward smooth, continuous, and mirror-like surfaces with increasing slip. We collected 123 scans of pristine slip surfaces, which measure surface geometry from micrometers to meters in length scale. Results indicate that slip surface roughness is systematically smoother than joint surfaces and deformation band edges. Over the best resolved length scales (0.1–10 mm), we observe roughness decreases with slip according to a power law with exponent −1 in the slip direction. Slip-perpendicular profiles, though rougher, exhibit the same smoothing trend. The Hurst scaling exponent does not change with slip. These observations require wear to be multiscale. Boundary element method models suggest that mechanical wear of completely mated surfaces occurs by asperity failure and that the wear rate depends on the aspect ratio of asperities. These results indicate that at large slip, asperity failure at all length scales can cause slip surfaces to smooth while maintaining the fractal geometry characteristic of faults.

Plain Language Summary Earthquakes occur on faults. It is known that fault geometry is a key factor to understanding earthquakes. This raises the following question: does fault geometry change from one fault to the other? It will likely be intuitive to the reader that the geometry may change as a fault accumulates displacement and rub past each other. However, measurements have yet to show that this is definitely the case for faults. This is because this measurement is difficult to obtain. In fact, laboratory experiments struggle to reproduce realistic conditions. We instead shift our attention to a natural laboratory, the San Rafael Desert, SE Utah, United States. In the study area, hundreds of *dead faults*, which were once active millions of years ago kilometers underground, can be found at the surface and cracked open using a chisel and hammer. Since all the faults are hosted in a geological context that is relatively consistent, we can isolate the effect of displacement on fault geometry. We measure their geometry with scanners. As expected, we find that faults that have experienced more displacement are smoother. Moreover, we see a clear transition from what are essentially cracks to faults so smooth that they have mirror-like surfaces.

1. Introduction

Offset across fault zones is localized onto one or many discrete slip surfaces (Aydin & Johnson, 1978; Engelder, 1974; Palmer & Rice, 1973; Sibson, 2003). These interfaces are not planar. Features such as slickenlines and jogs exhibit geometrical roughness at all scales of observation (Kirkpatrick & Brodsky, 2014; Sagy & Brodsky, 2009; Scholz & Aviles, 1986). Roughness therefore constitutes a population of geometrical protrusions on a slip surface, referred to as asperities (not be confused with seismological asperities; Lay et al., 1982). Fault roughness, and geometry in general, has a significant effect on fault and earthquake mechanics. Laboratory experiments comparing the behavior of smooth and rough surfaces show that increasing roughness causes a corresponding increase in frictional resistance (Biegel et al., 1992), critical slip distance, and rupture nucleation dimension (Ohnaka & Shen, 1999; Okubo & Dieterich, 1984) and fundamentally controls frictional stability (Harbord et al., 2017; Marone & Cox, 1994; Ohnaka, 2013). Large-scale numerical models incorporating realistic fault geometries show that slip surface roughness increases shear resistance (Fang & Dunham, 2013), directly affects rupture source parameters, and drastically limits the moment release of comparatively rougher

faults (Zielke et al., 2017). Accordingly, larger mega-earthquakes are observed to occur on smoother faults (Bletery et al., 2016).

Self-affinity, a form of fractal scaling, has been shown to capture the complex geometry of exhumed fault surfaces over a remarkably broad range of length scales (10^{-4} to 10^{7} m; (Bistacchi et al., 2011; Brodsky et al., 2016; Candela et al., 2012; Power et al., 1987; Renard et al., 2013; Sagy et al., 2007; Schmittbuhl et al., 1993; Scholz & Aviles, 1986). The magnitude and scaling behavior of fault roughness is quantified using a spectral decomposition of discretized 2-D profiles through a fault surface. When many profiles are averaged, the roughness is statistically well described by the scaling law:

$$P(\lambda) = C\lambda^{1+2H}, \tag{1}$$

where $P(\lambda)$ is the average power spectral density (PSD) of profiles through the slip surface at the wavelength, λ, C is a prefactor, and H is the scaling exponent (< 1 for self-affinity), also known as the Hurst exponent (Mandelbrot et al., 1984; Power & Tullis, 1991). Hurst exponents in the slip-parallel and slip-perpendicular directions of fault surfaces are ~0.6 and ~0.8, respectively. These geometric scaling exponents are robust to geological contexts and observational bandwidths, showing that fault roughness generally scales in a consistent manner (Brodsky et al., 2016; Lee & Bruhn, 1996). However, C, which determines the magnitude of roughness, varies by more than 5 orders of magnitude (e.g., Candela et al., 2012). The geological controls on this variability are largely unknown.

Detailed field investigations of exhumed faults identify a range of processes that affect slip surface geometry, inducing both smoothing (e.g., asperity failure and abrasive wear) and reroughening (e.g., sidewall ripouts and off-fault damage; e.g., Petit, 1987; Shervais & Kirkpatrick, 2016; Swanson, 1989). Theoretical arguments (Archard, 1953; Bowden & Tabor, 2001; Scholz, 1987), as well as indications of fault rock thickness increasing with slip (Robertson, 1982; Shipton et al., 2006), suggest a relation between removal of material from either slip surface (i.e., wear) and cumulative slip on the fault (Brodsky et al., 2011; Power et al., 1988). In support of this prediction, Sagy et al. (2007) noted a decrease in roughness of *mature* large-slip faults compared to *immature* low-slip faults. This relation is, however, only weakly apparent in compilations of fault roughness analyses (Brodsky et al., 2011; Candela et al., 2012), perhaps due to the combination of disparate data sets from different tectonic settings and rock types. Laboratory experiments that imposed shear across preexisting fracture surfaces in limestone blocks find that the amplitude of roughness decreases by a roughly constant fraction regardless of length scale (Davidesko et al., 2014). However, similar experiments at higher normal loads instead produced rougher surfaces with slip (Badt et al., 2016).

These results emphasize that challenges in scaling lab experiments to natural faults and combining univariate field observations of fault roughness make it difficult to relate roughness to cumulative slip. A measurable and systematic evolution in fault roughness would have considerable implications for fault behavior and would provide tools to better model the behavior of faults.

In this study, we use a combination of field, analytical, and numerical approaches to qualify, quantify, and explain the evolution of slip surface roughness. Well-preserved slip surfaces along faults exposed in the San Rafael Desert, Utah, which cut massive sandstone and formed under the same tectonic conditions, provide a natural observatory for isolating the effect of slip on roughness. Field and microstructural observations focus on recording qualitative changes in the characteristics and geometry of fault slip surfaces from initiation structures to small-slip faults (centimeters of slip) and finally to large-slip faults (tens of meters of slip). We present a geometric analysis of three-dimensional topography of pristine fault slip surfaces using data acquired in the field with a ground-based light detection and ranging (LiDAR) and a laser scanner and in the laboratory with a white light interferometer. Finally, using boundary element method models within a work optimization physical framework, we explore geometric sensitivity of single asperity failure. Combining all these components, we propose that a simple mechanical wear process acting across scales can explain the geometric evolution of slip surfaces.

2. Geological Context

The San Rafael Desert in central Utah hosts a sequence of gently dipping, Pennsylvanian to Jurassic, marine and subaerial sedimentary rocks. These formations are folded into a north-south trending monoclinal antiform, the San Rafael Swell, which formed as a passive drape fold above a basement reverse fault

Table 1
Overview of the Different Structures Analyzed in This Study

Structure	Lithology	Depth of faulting	Maximum offset	Sense of slip	Nucleation mechanism	Exposure type	Description
Chimney Rock Fault Array	Navajo Carmel Fm.	2–4 km	55 m	Normal Oblique	Joints (WNW) Deformation bands (ENE)	Scarp	Two mutually cross cutting conjugate sets of normal faults (Davatzes et al., 2003; Krantz, 1988; Maerten et al., 2001)
Big Hole Fault	Navajo	1.5–3 km	35 m	Normal	Deformation bands	Scarp cross section	Large normal fault with two major strands traceable along river wash (Shipton, 1999)
Hawk's Nest (Iron Wash)	Navajo Carmel Fm. Entrada Ss.	1–4 km	80 m	Normal oblique transform	Joints and deformation bands	Cross section	Complex network of faults at the intersection of Hawk's Nest and the Eastern Limb of Regional monocline (Aydin, 1977)
Molly's Castle	Entrada Ss.	1–2.5 km	12 m	Normal	Deformation bands	Scarp cross section	Conjugate E-W striking network of steeply dipping normal faults and deformation bands. (Aydin, 1977)

Note. Fm = formation; Ss. = sandstone.

reactivated during the Laramide Orogeny (66.4–37 Ma; Kelley & Clinton, 1960; Krantz, 1988; Vrolijk et al., 2005). Approximately synkinematic networks of joints and normal faults cut the sedimentary sequence and generally accommodated north-south extension (Aydin, 1977; Kelley & Clinton, 1960).

We focused on the following structures: the Chimney Rock Fault Array, Big Hole Fault, Hawk's Nest Fault, which outcrops in the Iron Wash, and an array of small faults near Goblin Valley State Park (refer to Table 1 for structure-specific information and Figure 1 for a map overview). These faults were all active during the Laramide Orogeny and cut the Navajo Sandstone (Lower Jurrassic), the Carmel Formation (Middle Jurrassic), and the Entrada Sandstone (Late Jurrassic). Statigraphic thickness estimates place the sequence at 1- to 4-km depth during Laramide activity in and around the San Rafael Swell (Davatzes, 2003; Doelling & Willis, 2008; Fossen et al., 2011; Shipton, 1999). Available stratigraphic evidence suggests minimal differences in burial depths of the formations and inferred depth of faulting in the different study areas (Johansen & Fossen, 2008). The Navajo Sandstone is a massive, 150-m-thick, well-sorted, well-cemented, and highly porous quartz arenite with a mean grain size of ~0.1 mm (Aydin, 1977). It is composed of 90% quartz, 10% feldspar, and trace (<1%) ferromagnesian minerals with calcite and silica cements. The Carmel Formation is a ~50-m-thick sequence of limestone, siltstone, and sandstones interbedded at the decimeter scale (Aydin, 1977). Finally, the Entrada Sandstone is a >150-m-thick well-sorted yellow-gray quartz arenite, slightly more friable than the Navajo Sandstone, with a mean grain size of ~0.2 mm punctuated by siltstone and shale horizons (Aydin, 1977; Bright, 2006). The unit is dominantly composed of quartz with trace feldspar and ferromagnesian minerals. Both massive sandstone units host well-defined meter-scale cross beds with centimeter-spaced cross strata.

In the Navajo and Entrada Sandstones, fault nucleation occurred through reactivation of deformation bands or joints formed during the initial stages of deformation. Deformation bands are characteristic structures in porous rocks deformed at shallow burial depths (e.g., Fossen et al., 2007). They form wavy sheets typically less than a few millimeters thick in which grain comminution and the concomitant collapse of pore space accommodate strain, predominantly in shear, on the order of unity (Fossen et al., 2007; see example in Figure 2a). Deformation bands form at low bulk strain in porous rocks; when the host rocks are further deformed, deformation bands form adjacent to each other and develop into dense networks of closely packed anastomosing bands called deformation band clusters (Aydin, 1977; Aydin & Johnson, 1978), which are more compacted

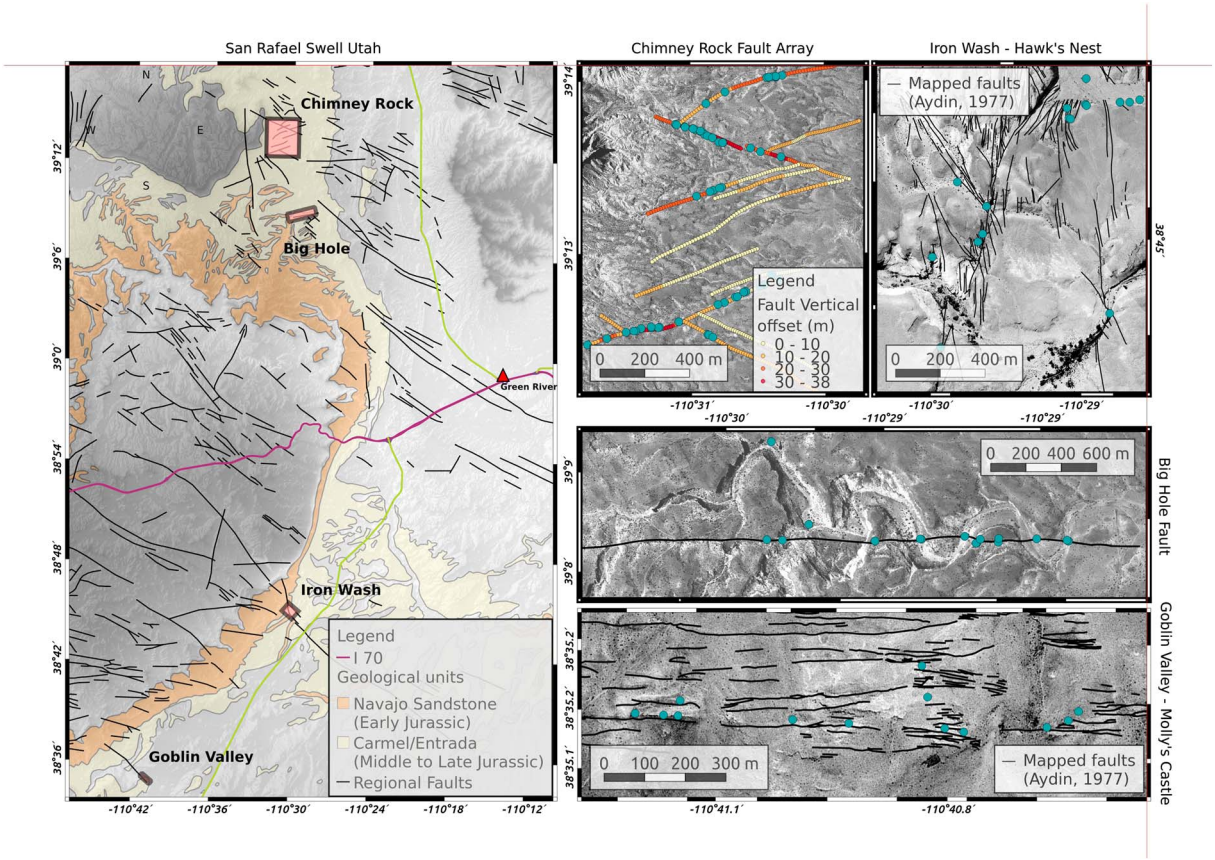

Figure 1. Field areas featured in this study. (left) Map of the San Rafael Desert, Utah. Geological metadata obtained at 1:500,000 scale from Ludington et al. (2007). Field locations featured in this study are indicated by pink boxes. (right) Small-scale maps of each field location. Faults (black lines) are superposed on Digital Orthophoto Quadrangle areal imagery made available by U.S. Geological Survey. Blue points indicate locations where faults were scanned and sampled. (middle top) Chimney Rock Fault Array with estimates of vertical fault offset from Maerten et al. (2001). (top right) Field map from Aydin (1977) of the Iron Wash exposure of the Hawk's Nest fault system. (middle right) The Big Hole fault. (bottom right) Detailed map from Aydin (1977) of the faults near Molly's Castle in Goblin Valley.

and indurated than the sandstone protolith (Antonellini et al., 1994; see example in Figure 2b). Following the formation of deformation band clusters, minor slip surfaces form in and along their edges. Minor slip surfaces link and, ultimately, form one or more major slip surfaces that accommodate the majority of slip and form a well-defined fault core (Aydin & Johnson, 1978; Bright, 2006; Shipton & Cowie, 2001).

Fault nucleation in the Navajo Sandstone has also been shown to have occurred through the reactivation of preexisting and syntectonic joints (Davatzes et al., 2003; Myers, 1999). Slip across reactivated joints causes the formation of additional sheared joints at their tips and zones of fragmentation up to meters in thickness, through which faults link to form throughgoing slip surfaces and, eventually, mature fault zones (Davatzes, 2003).

3. Field and Microstructural Observations of Slip Surfaces

3.1. Initiation Structures

Deformation bands typically form sinuous white lineaments in cross-sectional exposures. Thin section observations show a gradational, roughly tenfold reduction in grain size and porosity toward the center of the bands. Exposed faces that bound deformation bands are wavy and coated with grains of sand from the adjacent protolith. Outer surfaces of deformation band clusters display a three-dimensional corrugated morphology (see Figure 2b). The surfaces are lobate, exhibiting repeated sets of arcuate bends, around a centimeter in amplitude, terminating inward in sharp cusps at 1- to 10-cm intervals in horizontal exposures perpendicular to slip. Surfaces that face the hanging wall preserve protrusions that taper and broaden downdip; conversely, the updip terminations are relatively sharp and abut steeply into the next corrugation. Similar to individual deformation bands, these surfaces are always coated with a cohesive,

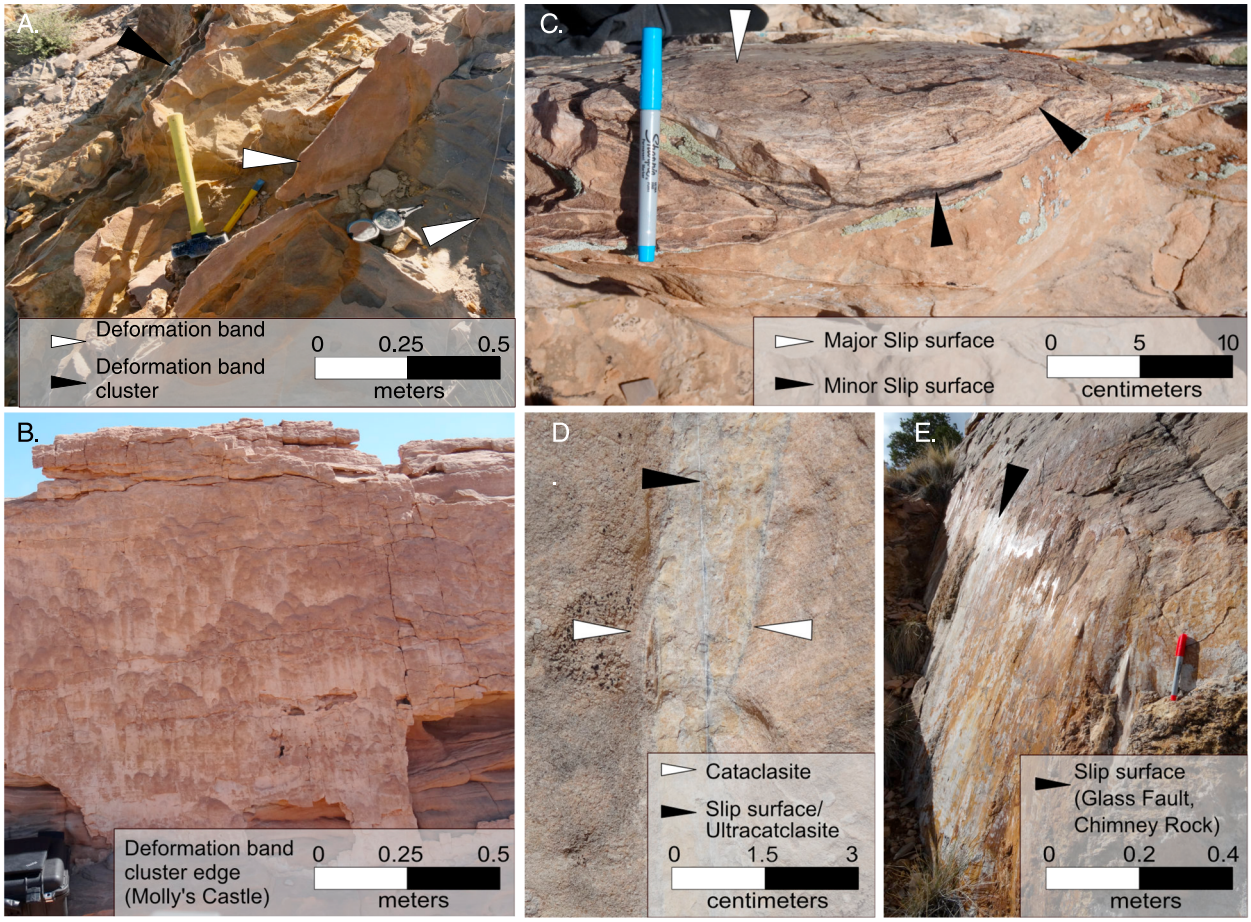

Figure 2. (a) Deformation bands protruding out of outcrop as thin sheets of cemented comminuted sand grains (Molly's Castle). (b) Edge of deformation band cluster (D = 16 cm) with distinctive lobate morphology and asymmetric termination (Molly's Castle). (c) Slip-perpendicular cross section of the major slip surface on the footwall with minor, likely abandoned, slip surfaces forming concentric patterns (Big Hole Fault, D = 7.8 m). (d) Slip-perpendicular cross-sectional view of slip surface with characteristic thin, submillimeter layer of white ultractaclasite and broader, centimeter-wide zone of cataclasite grading into a zone of dense deformation bands (Hawk's Nest, D = 24 cm). (e) Well-exposed plan view of slickensided faults with mirror-like polish (Glass Fault, Chimney Rock Fault Array, D<27 m).

single-grain-thick layer of undeformed sand grains from the host sandstone. Joint surfaces are notably smoother than deformation bands but rougher than slip surfaces. Morphological features on joint surfaces, all with subcentimeter amplitude, include plumose structures, which are curved and form approximately radially symmetric sets and intersection lineations aligned with cross-bedding horizons.

3.2. Slip Surfaces

Slip surfaces in the Navajo and Entrada Sandstones are consistently slickensided, exhibiting a polished, sometimes reflective, lustre (see Figure 2e). They readily form subplanar parting surfaces, indicating that cohesion across them is low. Slip surfaces are most commonly white but can also be dark gray, reddish-brown, yellowish-beige, or grayish-beige. Some surfaces have distinct patches with different colors elongated in the direction of slip. Dark oxide phases, typically associated with millimeter-sized depressions, form <1-mm circular, radially dendritic, growth patterns on some slip surfaces.

Following terminology in Hancock and Barka (1987), we use scratches, grooves, tool tracks/gutters, and corrugations, respectively, 1, 20, 40, and >50 mm in width, to describe slickenlines of varying length scales. All can be generally described as surface depressions strongly elongated in the inferred direction of slip. When best defined, scratches form thin lineaments that taper out at either end over distances of a few centimeters. Grooves, tool marks, and gutters typically form broader U- or V-shaped indentations viewed in the slip-perpendicular direction and can persist along the direction of slip for tens of centimeters. Slickenlines sometimes taper out asymmetrically with steeper, more abrupt, and narrow ends in the direction of slip.

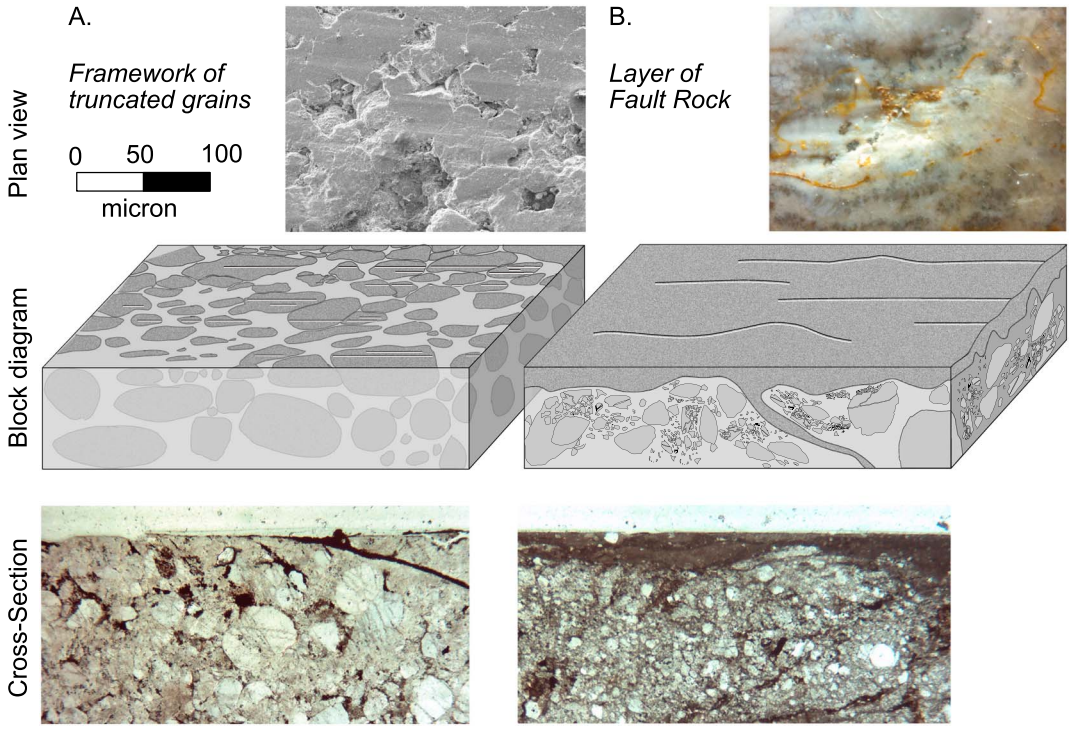

Figure 3. Representative three-dimensional depiction of two mature slip surface end-members in plan view (top), in schematic block diagram (middle) and in cross section with plain polarized thin sections (bottom). (a) Slip surface cutting relatively undamaged protolithic grains. Plan view obtained using scanning electron microscopy shows truncated grains with through going striae. Note that protolithic textures can still be identified in thin section. (b) Slip surface overlying ultracataclasite, which in turn overprints cataclasite. Plan view image taken optically through the microscope.

Multiple slip orientations are preserved on some slip surfaces, whereby broad gutters align in one direction and finer scratches align obliquely to this dominant set (up to 40° in obliquity). We observed up to three different orientations on single slip surfaces, though the vast majority of surfaces preserve only one dominant direction.

The faces of slip surfaces preserve two different structural styles (see Figure 3). In some cases, surfaces are made up of frameworks of flattened grains, ranging from rounded (likely corresponding to the protolith) to highly angular (Figure 3a). Flattened grains are cut by even finer discrete striae, which project linearly across multiple grains. Alternatively, slip surfaces are composed of a white, beige, or gray, sometimes semitranslucent and glassy, fault rock layer (Figure 3b). Isolated, rounded to highly angular grains are perceivable on the surface and within the fault rock. Both styles, along with a heterogeneous patchwork of both components, occur both on large- and small-slip faults. Slickenlines are superposed onto all styles of surfaces.

In cross-sectional exposure, the surface traces of slip surfaces are discrete, throughgoing and smooth relative to joints and deformation bands. In all cases, perpendicular profiles are notably more sinuous than corresponding slip-parallel profiles. Sections viewed perpendicular to slip surfaces and parallel to slickenlines reveal a layered microstructural architecture of the fault rocks locally bounding slip surfaces. We find the following components commonly bound slip surfaces: (1) a very fine-grained ultracataclasite layer, (2) a broader cataclasite layer, and (3) a deformation band zone, the density of which gradually decreases into (4) the relatively intact protolith with disparate deformation bands. While the relative ordering of these components is consistent across our sample suite, some, or even all, can be absent.

The ultracataclasite layer that bounds the slip surface tends to be nearly continuous, crosscuts all other layers, and ranges from $<$ 1 to 2 mm thick. The slip surface itself defines an abrupt and nearly straight edge to this layer. The ultracataclasite contains a few visible randomly oriented, subrounded to angular clasts not exceeding tens of micrometers long in a matrix that is mostly unresolveable at 400-fold magnification. We were unable to find fragmented counterparts within the ultracataclasite, indicative that the layer was mobile or even fluidized (Otsuki et al., 2003). Fractures crosscutting the entire ultracataclasite layer indicate at least

one cycle of healing and brittle failure postdating the formation of ultracataclasite. Planed-off clasts at the slip surface edge of the ultracataclasite further support this interpretation.

The cataclasite has a higher proportion of large clasts compared to the ultracataclasite, and the maximum grain size is larger (typically a few tens of micrometers long). Bands or lenses of larger clasts are separated by finer, more angular clasts, texturally similar to deformation bands. Cataclasite layers range from being completely absent to being a few centimeters thick with substantial local variability often asymmetric with respect to the slip surface. Fractures that splay from the slip surface, also bounded by cataclasite, increase the cataclasite layer thickness. While the ultracataclasite can occur in the absence of a cataclasite layer, the opposite is not observed in our sample suite. In the absence of either layer of fault rock, truncated grains form a continuous and relatively planar slip surface trace.

A sharp, irregular, and discontinuous interface consistently juxtaposes the cataclasite layer and the ultracataclasite. The interface is defined by a distinct change in clast size and spatial arrangement. The interface between cataclasite and ultracataclasite is either lined by clasts that locally protrude into the ultracataclasite or clasts that were truncated at the interface (see Figures 4a and 4b). Clasts exhibit various stages of microcracking. Fractures are roughly parallel to the slip surface and sometimes host minor shear offset and/or rotation. Most often, clasts are fully parted with fragmented counterparts completely absent.

Some intragranular fractures are aligned and project into neighboring grains forming larger millimeter- to centimeter-scale arcuate, intergranular fractures with ends abutting in the ultracataclastic layer with shallow obliquity (see Figure 4c). The abundance of these fractures seems to be anticorellated with the thickness of the ultracataclasite. This geometry is recorded at various stages: roughly aligned but discontinuous intragranular fractures; partially parted lenses with well-defined and fully connected fractures; and the completely removed lenses (as evidenced by the geometry of the ultracataclasite-cataclasite contact). This scalloped geometry, though exhibited here at a smaller scale, is similar to *sidewall ripouts* described by Swanson (1989).

Slip surfaces with the microstructural architecture described above can either occur in isolation or be nested in larger, more complex fault zones. Fault zones contain multiple minor slip surfaces, as well as one or more major slip surfaces (see Shipton et al., 2005, for further description of fault zone architecture). In isolation, the layering associated with a single slip surface rapidly grades into nearly intact undeformed sandstone.

3.3. Slip Surface Maturation

3.3.1. Immature Slip Surfaces

Our observations suggest key structural elements of fault slip surfaces change with slip. Slip surfaces with tens of centimeters slip or less are visibly more sinuous in cross-sectional exposures. They are laterally discontinuous and are commonly arranged in complex linkage structures, splays, or crosscut synthetic conjugates. The minimum observed offset across slip surfaces was ~0.5 cm. On slickenside surfaces, small-slip faults are consistently strongly striated with well-defined scratches. Grains protrude from the surfaces. The maximum size of the grains is similar to the host rock, but most are smaller. Samples collected along minor slip surfaces within fault zones that also contained a well-developed, throughgoing surface preserve elongated striae with millimeter width and height. Some striae are composed of consolidated white fault rock, with widths roughly equivalent to protruding grains, and appear to form *tails* opposite to the direction of slip, which taper or link up with other protruding grains. This slickenline morphology is consistent with descriptions of *erosional sheltering* (Means, 1987) or *trailed material* (Doblas, 1998). Small-slip surfaces are consistently less polished, typically exhibiting a dull lustre. They inherit characteristics from nucleation. For example, deformation band faults are white; faults that nucleated from sheared joints are pale beige with abundant black oxide phases. A thin layer of fault rock commonly bounds the slip surfaces in spite of minimal slip.

3.3.2. Mature Slip Surfaces

Slip surfaces with slip $> 10^0$ m are noticeably more discrete, sharp, and planar in 3-D exposure. We only observed pristine, vitreous, and mirror-like slip surfaces along major fault surfaces in the Chimney Rock Fault Array (where upper-bound slip exceeds tens of meters), the main strand of the Big Hole Fault where slip was 20 to 35 m and a minor slip surface with at least 3-m slip of the Big Hole Fault. Mirror-like slip surfaces tend to be less clearly striated than their small-slip counterparts. Grains do not form protrusions on these surfaces. Scratches formed within the vitreous translucent outer layer of fault rock in most exposures we studied. However, some centimeter-sized samples have no visible grooving or striations. The intensity of striations is spatially variable on a single slip surface such that in some cases finer striations appear to cluster in small square centimeter-sized local depressions on the slip surface. Large-slip slip surfaces are consistently bounded

by a well-defined layered fault rock architecture (as described above). Our qualitative observations tentatively suggest the mobile ultracataclasite layer thickness increases (up to ≈ 3 mm) with slip.

Larger-scale and more complex macroscopic fault architecture is nearly always associated with faults that have larger offset. Multiple subparallel slip surfaces partition the stratigraphic offset that is accommodated by the fault zone as a whole (e.g., see Shipton & Cowie, 2001). Smaller, discontinuous, and notably more sinuous slip surfaces occur on either side and sometimes abut into, throughgoing, more planar slip surfaces. Large-slip slip surfaces are never crosscut by any other feature in the fault zone (e.g., minor slip surface, joint, or deformation band), providing both key criteria for identifying major large-slip slip surfaces in the field and a signature of the temporal evolution of the fault system.

4. Measurements of Fault Roughness

4.1. Data Acquisition

To measure the roughness of fault slip surfaces, we collected high-precision, high-density measurements with a desktop laser scanner and ground-based LiDAR in the field and, later, in the laboratory, on hand samples with a while light interferometer. See the supporting information for instrumental details. Hand samples comprise both a subset of the faults measured in the field and additional slip surfaces where only smaller areas of pristine surface were exposed. As a result, the smaller-scale laser scanner and laboratory measurements constitute the bulk of the data. LiDAR data, being the primary method to collect fault roughness measurements to date (Brodsky et al., 2011; Candela et al., 2012; Jones et al., 2009; Kirkpatrick & Brodsky, 2014; Renard et al., 2006; Sagy & Brodsky, 2009; Sagy et al., 2007), were collected to ensure that faults in the study areas are consistent with the fractal paradigm of fault roughness and that geometric scaling is well captured with our other instrumentation.

We quantified roughness by averaging the PSD computed using a 1-D fast Fourier transform for hundreds or thousands of 2-D topographic profiles obtained from each surface scan (Schmittbuhl et al., 1993). Following Schmittbuhl et al. (1993), we distilled spectra to their prefactor and Hurst exponent by performing a linear regression through the log-transformed spectra (equation (1). Throughout this procedure, considerable effort was made to ensure that physical and instrumental artifacts (e.g., cracks, surfaces defects, instrumental noise, and instrumental filtering) did not affect results. Refer to the supporting information for detailed preprocessing, processing and analysis procedure (Brodsky et al., 2011; Candela et al., 2009; 2012; Lee & Bruhn, 1996; Schmittbuhl et al., 1993; 1995; Trauth et al., 2007).

We estimated the slip across every scanned slip surface based on previously published slip and throw profiles and field observations. For the Chimney Rock Fault Array, we used a fault stratigraphic separation model that utilized high-resolution geospatial data with 1-m precision reported in Maerten et al. (2001). At Big Hole, we used maps of fault architecture that indicate stratigraphic offset constrained from total station surveys as a reference (5-m precision due to uncertainty in measurements of bedding attitude; Shipton & Cowie, 2001). At Iron Wash, Horse Creek, and Molly's Castle, we revisited the offset markers identified by Aydin (1977) and added new slip constraints using marker horizons and slip vectors defined by slickenlines.

Slip across fault zones is partitioned onto major and minor slip surfaces, complex networks of deformation bands, and sheared joints, complicating the procedure for measuring values for individual slip surfaces. Here we make a distinction between *offset* across an entire fault and *slip* across a single slip surface. Without clear marker horizons and cross-sectional exposure, determining how multiple slip surfaces partition the stratigraphic offset can be ambiguous. Offset across the entire fault zone is therefore an upper-bound constraint on slip across a single slip surface. For 60% of our slip surface scans, this is the best available constraint.

We were able to reconstruct true slip on individual slip surfaces in the following cases: (1) if cross-sectional exposure indicated only one slip surface within a fault zone or (2) where a cutoff surface and slip vector were exposed (lamella, cross bedding, or lithological contact); or 3) if a fault zone unambiguously contained a *principal slip surface* that accommodated the overwhelming majority of fault offset; that is, one slip surface was continuous, had an associated layer of fault rock, and was unmistakably sharp and linear compared to any other slip surface in the fault zone (following Chester & Logan, 1986, and in our field area, Shipton & Cowie, 2001). We report a conservative 10% error on field-based slip estimates based on measurement uncertainties in the strike and dip and apparent offset.

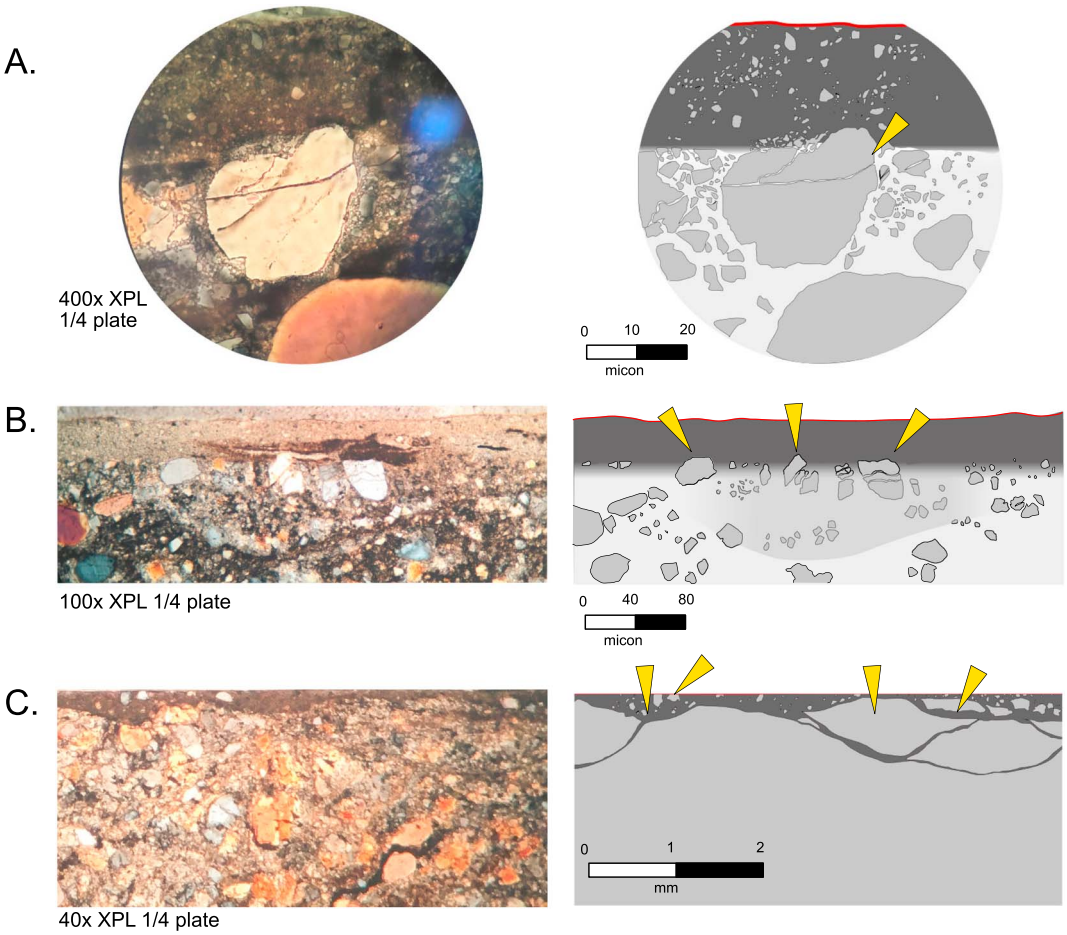

Figure 4. Microstructure of damage on and near the interface between the ultracataclasite and the cataclasite (photomicrographs taken with a one-fourth wavelength phase shift to help highlight key microstructural features). The right column shows an interpretive depiction of key microstructural elements. Red line indicates the preserved slip surface; dark gray indicates the ultracataclasite layer; pale gray indicates the cataclasite. Yellow arrows draw attention to important elements. (a) A relatively intact grain protrudes into the ultracataclasite (400-fold magnification). Note the fracture completely crosscutting the grain. (b) Grains at the interface with the ultracataclasite with various levels of internal damage (100-fold magnification). Arrows from left to right: nearly intact grain with slightly planed off top; intensely damaged grain, which is beginning to rotate into the ultracataclasite; intact but damaged grain with top missing a fragmented counterpart. (c) Scalloped interface between cataclasite and ultracataclasite (40-fold magnification). Arrows from left to right: scalloped and fully removed section of the cataclasite; grain at the slip surface interface that is planed off; intact lens of cataclasite isolated by arcuate fracture; nearly removed section of cataclasite beginning to be comminuted into the ultracataclasite.

4.2. Results

Figure 5 shows the PSD spectra obtained from all of the scans collected in this study. Scans using the laser scanner yield Hurst exponents that are relatively evenly spread in the range from 0 to 1.1 with an average value of 0.5 in the slip-parallel direction and 0.1 to 1.2 with an average value of 0.6 in the slip-perpendicular direction. Scans using the white light interferometer yield exponents between 0 to 1.2 with an average value of 0.4 in the slip-parallel direction and 0 to 1.6, with a mean value of 0.7 in the slip-perpendicular direction.

The spectra shown in Figure 5 qualitatively indicate that roughness measured in both the slip-parallel and slip-perpendicular directions correlates with slip. Joints and deformation bands, the structures associated with the initial nucleation of a fault, are systematically rougher than the slip-parallel roughness of fault, but some are rougher in the slip-perpendicular direction. Additionally, fault surface PSD at any wavelength tends to decrease (while always fractal) with increasing slip. The Hurst exponent of the spectra does decrease slightly with increasing slip for the scans collected with the laser scanner, but this trend is not apparent in spectra obtained from scans using the white light interferometer. Over our entire data set, the Hurst exponent does

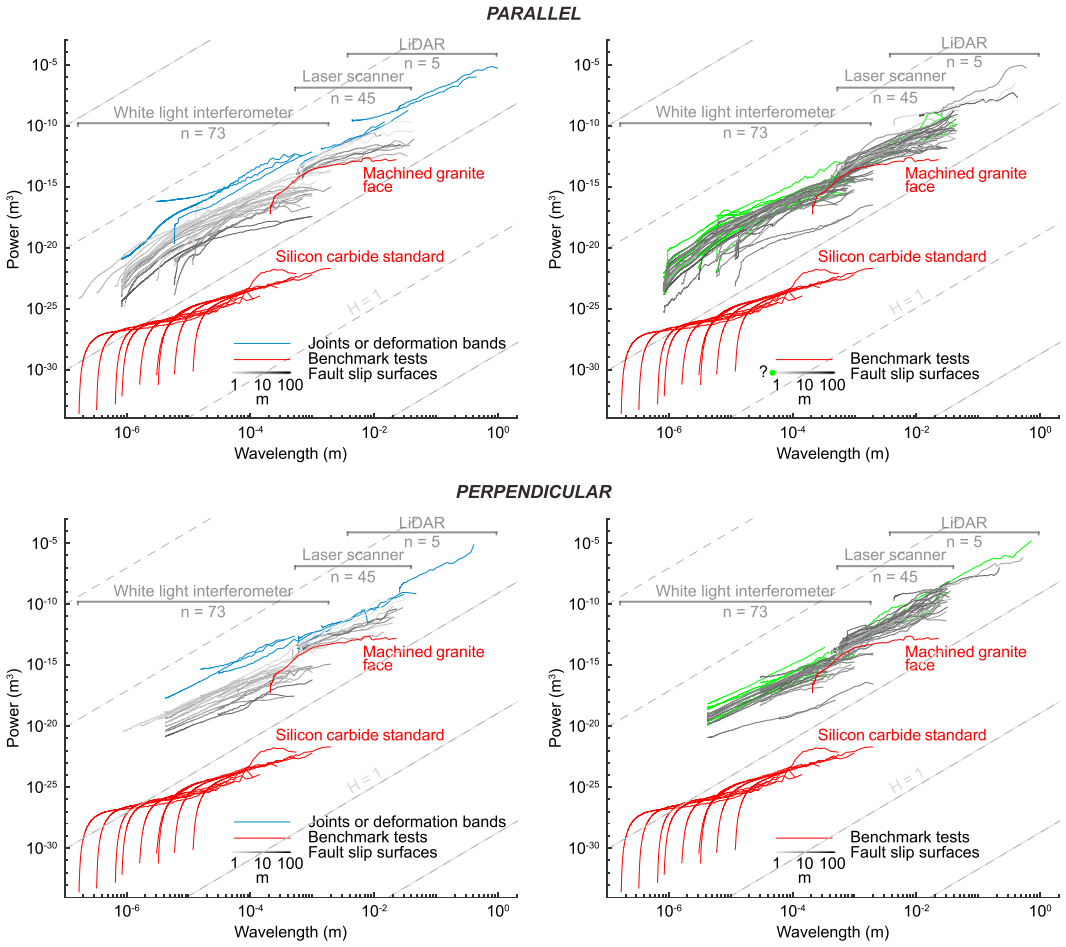

Figure 5. Roughness spectra in the slip-parallel (top row) and slip-perpendicular (bottom row) direction for all scans collected with the white light interferometer (spectra with wavelengths up to 10^{-3} m), laser scanner (spectra with wavelengths from 10^{-4} to 10^{-1} m), and ground-based LiDAR (spectra with wavelengths from 10^{-2} to 10^{0} m). Blue lines correspond to scans of joints and deformation bands. Spectra computed for slip surfaces with a slip estimate are graded logarithmically according to increasing slip from pale gray to black. (left column) Spectra were computed from scans with direct slip constraints. (right column) Spectra were computed from scans with in direct constraints where the color indicates the maximum offset. Green lines represent spectra with unknown slip. Red lines corresponded to silicon carbide planar reference for white light and machined-flat granite reference for laser scanner. Note that the low-wavelength tails that fall off in power are instrumental artifact and are not considered in subsequent analysis. LiDAR = light detection and ranging.

not correlate with slip (Figure 6). Building upon the approach used by Brodsky et al. (2011), we use data with direct slip constraints to serve as (1) a direct test of a correlation and (2) a means to parameterize an empirical power law smoothing model, whereby

$$P(D, \lambda = L) = AD^{B}, \tag{2}$$

where P is the PSD, D is the slip, λ is the wavelength, L is an interpolation length scale, A is a constant of proportionality, and B is the smoothing exponent. We obtained the power at a given length scale ($\lambda = L$) from the fit to the data with equation (1) and the fractal parameters calculated from the scan to overcome noise in the PSD spectra.

We used roughness measurements associated with a direct constraint on slip to define an empirical power law smoothing model from a least squares linear regression through three log-transformed data sets evaluated at $L = 10^4$, 10^3, and 10^2 m (Figure 7). The 1σ error bounds on the fit parameters are determined with full Monte Carlo and bootstrap resampling simulations (1,000 simulations). In the slip-parallel direction, we find that a power law smoothing model yields variable constants of proportionality but relatively consistent smoothing exponents of -0.9 ± 0.4, -1.0 ± 0.5, and -0.5 ± 0.3, respectively, for the three length scales evaluated. P values respectively indicate a 99.4%, 99.5%, and 98% confidence that smoothing exponents are nonzero. The

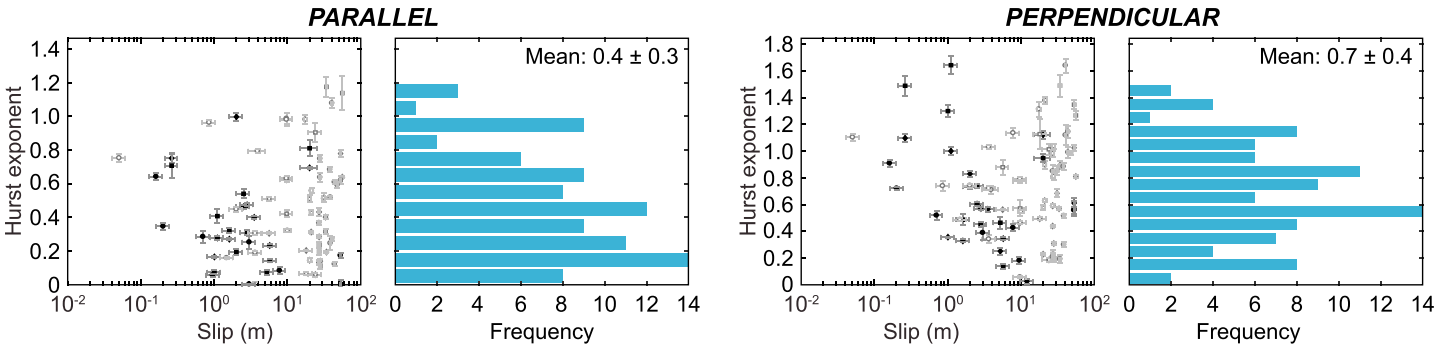

Figure 6. Hurst exponents as a function of slip in the slip-parallel (left pair) and slip-perpendicular (right pair) direction. Black and white points respectively indicate data associated with direct and fault offset constraints on slip. Data is shape coded according to the instrument and magnification used to obtain Hurst exponents. Black and white points, respectively, indicate data associated with direct and fault offset constraints on slip. Vertical error bars are 1σ uncertainty intervals in from the fractal model fit. Error on slip is considered on a case-by-case basis (see section 4.1).

conjugate analysis in the slip-perpendicular direction yields similar results with exponents of -1 ± 0.3, -1.0 ± 0.4, and -0.5 ± 0.4 on the smoothing trends at 10^{-4}, 10^{-3}, and 10^{-2} m, respectively. P values respectively indicate a 99.9%, 99.9%, and 92% confidence that smoothing exponents are nonzero.

Considering the inequality $P(D, \lambda = L) = A(D_{max} - \epsilon)^{\beta} < AD_{max}^{\beta}$, where D is actual slip, D_{max} is maximum slip and $\epsilon > 0$ is unknown, scan data only associated with upper bound constraints on slip provide nearly systematic support for the smoothing model. This is shown graphically in figure 7 where nearly all points, (P, D_{max}), fall above the best fit line fit through the former data set.

We recognize that (1) scatter relative to the regression much exceeds uncertainty for individual measurements and 2) there is considerable variability in the estimated smoothing exponents (propagated from individual fault slip surface measurements).

Variability in smoothing exponents , especially across various scales of observation, is likely in part explained by limitations of the laser scanner, which yielded a lower smoothing exponent than the white light interferometer in both directions at $L = 10^{-2}$. Instrumental accuracy approaching the topographic variance of some of the smoothest slip surfaces potentially resulted in overestimates of roughness and an underestimation of the Hurst exponents because of superposed instrumental noise signals. Moreover, reroughening induced by erosion and surface degradation (Brodsky et al., 2011) is likely to disproportionately affect the larger slip surfaces scanned with the laser scanner. Together, we expect that these effects would result in an underestimated smoothing exponent obtained from the laser scanner data. Neither artifact should be significant for white light interferometer, where smaller samples were, comparatively, consistently more pristine. White light instrumental accuracy is well below the topographic relief of fault surfaces (as shown in Figure 5).

While artifacts outlined above in part explain discrepancies across our scales of observation, they do not explain the scatter that occurs at any given length scale. The spread in roughness measurements of slip surface for a given slip has, in the past, been interpreted to be the result of other geological variables such as depth of faulting, faulting mechanism, and lithology (Brodsky et al., 2011; 2016; Candela et al., 2012; Sagy et al., 2007). However, these variables are all effectively held constant in this study. This leads us to suggest scatter in our data occurs in large part because we did not sample a representative elemental area of the surface at which the statistical properties of the height field would not vary spatially. This interpretation is supported by PSD estimates on different sections of a slip surface, even on a single slip surface hand sample, sometimes spanning more than an order magnitude. It is unclear from our measurements what sample sizes would be required to achieve a representative elemental area of the slip surface.

Given possible systematic bias for the laser scanner and large scatter in the data, we suggest a reasonable approximation is that fault slip surfaces featured in this study smooth in both the slip-parallel and slip-perpendicular directions according to a single power law with a fixed exponent of approximately -1 in both slip-parallel and slip-perpendicular directions. This implies that the ratio of roughness in the slip-parallel and slip-perpendicular direction (anisotropy) remains roughly constant with slip.

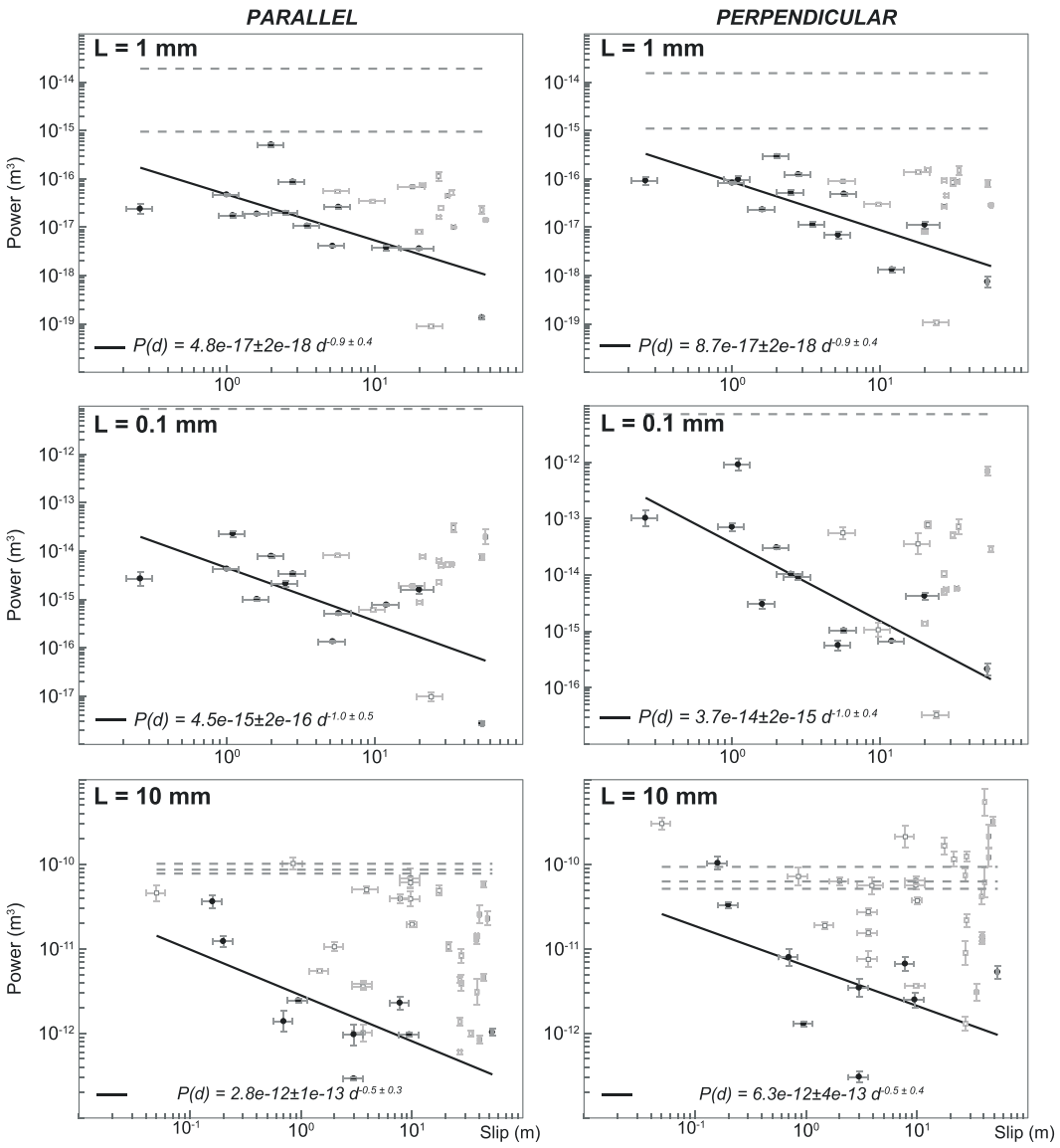

Figure 7. Correlation of roughness as a function of slip at three well-constrained length scales. Black and white points respectively indicate data associated with direct and fault offset constraints on slip. Best fit line indicated in black (equations relating power ($P(d)$) to slip (d) with uncertainties determined from Monte Carlo simulation with bootstrap resampling). Vertical error bars are 1σ uncertainty intervals in from the fractal model. Error on slip is considered on a case by case basis (see section 4.1). Roughness of joints and/or deformation bands indicated with gray dashed line. For clarity, power spectral density of silicon carbide reference surfaces is not shown as it falls below the minimum value shown on the plots for $L = 10^{-4}$ and $L = 10^{-3}$.

We infer that the fault smoothing defined by equation (2) is captured in the scaling prefactor (C) of equation (1) because of the invariance of the Hurst exponent with respect to slip (Figure 6) and the relatively consistent value of the exponent, B (Figure 7). The same considerations suggest fault anisotropy and corresponding scaling is captured in the A parameter. We can therefore generalize equation (2):

$$P(\lambda, D) = kD^B \lambda^{(1+2H)}, \tag{3}$$

where k is a constant. Note that that product kD^B is the prefactor, C, from equation (1). We take the geometric mean of every measurement of roughness (p_i) and Hurst exponent (H_i) associated with a direct constraint on slip (d_i) at each length scale presented above, $\bar{k} = \left(\Pi_{i=1}^{N} \frac{p_i(\lambda=L,d_i)}{d_i^{B\,|2H_i+1}}\right)^{1/N}$, which yields $k \approx 6 \times 10^{-10}$ in the slip-parallel direction and 9×10^{-8} in the slip-perpendicular direction. Using Parsevals theorem, following

Brodsky et al. (2011), the above relationship can be expressed in terms of the root-mean-square (RMS):

$$\mathrm{RMS}(L, D) = \sqrt{\frac{k}{2H}} D^{0.5B} L^{H}. \quad (4)$$

Equations (3) and (4) allow the roughness of a fault from our study area to be estimated at any slip and enable us to compare our results to other studies (Brodsky et al., 2016; Sagy et al., 2007). The Hurst exponents we report are similar to those found in previous work (Candela et al., 2012), so if the values of B and k are transferable to faults in other settings, these equations may define roughness as a function of slip generally.

5. Discussion

5.1. Do Faults Smooth With Slip?

Our results show with statistical certainty that within the first tens of meters of slip faults smooth in both the slip-parallel and slip-perpendicular directions. The weak sensitivity to slip reported in Brodsky et al. (2011), along with experimental evidence fault reroughening (e.g ; Badt et al., 2016), has led previous studies to suggest that fault roughness is a steady state between smoothing processes and reroughening (e.g., Brodsky et al., 2016; Candela et al., 2012; Fang & Dunham, 2013; Shervais & Kirkpatrick, 2016). However, we report an RMS-smoothing exponent of $0.5B$ (from equation (4), which is 5 times greater than that reported in Brodsky et al. (2011). It is possible that the large RMS-smoothing exponent is only representative of small-offset faults. The maturation of damage zones (Shipton & Cowie, 2001; 2003; Shipton et al., 2002), the effectiveness of reroughening processes (Brodsky et al., 2011; Shervais & Kirkpatrick, 2016), and formation of thicker packets of fault rock (Scholz, 1987) may all alter the smoothing and wear processes during slip. Taken at face value, the discrepancy between our measurements and those in Brodsky et al. (2011) could indicate a transient state in the immature stages of faulting (e.g., running-in proposed by Power et al., 1988; Wang & Scholz, 1994) or the onset of new processes at larger slips potentially driving fault roughness toward a steady state. Two insights from our results suggest that the high RMS-smoothing exponent is characteristic rather than transient.

First, we can assess the evolution of the smoothing behavior over the range of fault slips from nucleation (on the order of 1 or 2 cm) to 55 m. At slip comparable to offset across individual deformation bands, $\sim 10^{-2}$ m, the smoothing trends in Figure 7 indicate that fault roughness, in both slip-parallel and slip-perpendicular directions, closely approximates that of deformation bands and joints. At large slip, the power law implies a rapidly decreasing smoothing rate that asymptotically approaches 0. The extrapolation of our roughness-slip relationship (equation (4) to large slips yields roughness comparable to other data (e.g., Candela et al., 2012). These observations indicate that fault smoothing begins immediately following fault nucleation and persists throughout the development of the fault, with no requirement in the data for step change, run-in, or transient mechanics.

Second, the consistency of smoothing exponents in equation (2) estimated at different length scales is a natural extension of the fractal paradigm for fault slip surfaces (i.e., Candela et al., 2012; Mandelbrot, 1985; Schmittbuhl et al., 1993; Scholz & Aviles, 1986). A single smoothing exponent at all scales maintains the fractal character of the surfaces and does not affect the Hurst exponent (as shown in Figure 6). As Hurst exponents are well documented to be consistent for a wide variety of different faults (Brodsky et al., 2016), our results are in agreement with previous studies. The direct implications of this insight are that (1) a single mechanical process may dictate the geometry of the slip surface (Dimri, 2000), wherein (2) the fractional change in roughness during an increment of slip must be independent of scale.

We obtain good agreement with the results in Brodsky et al. (2011) when considering the power law model of fault RMS roughness as a function of total fault *offset* (as opposed to *slip* in a single surface). This treatment yields a substantially worse correlation since it is effectively an analysis of the smoothness of a random slip surface within a fault zone where each slip surface partitions an unknown fraction of total fault offset. While partitioned slip is likely to induce ambiguity for the small faults presented in this study, it is less likely to be the case faults with large $> 10^2$-m fault offset as mature faults tend to localize slip onto major slip surfaces, often referred to as principal slip surfaces (e.g., Caine et al., 1996; Chester & Logan, 1986; Sibson, 1977; Shipton & Cowie, 2001). Nevertheless, we suggest that the discrepancy in analytic treatment plays an important role in explaining both the extensive scatter and the underestimation of the smoothing rate of Brodsky et al. (2011) relative to our results.

5.2. Slip Surface Processes

A variety of structures evident in the field and microscopic observations changed the geometry of the fault surfaces we studied.

Our observations (e.g., Figures 3 and 4) show that during slip, fault rock was formed and mobilized to redefine the geometry of fault surfaces. Mobile fault rock is evidenced by missing fragmented counterparts, extreme grain size reduction, and trailed slickenlines within and at the edge of the ultracataclasite layers. However, the ultracataclasite was also lithified during deformation. The edges of the ultracataclasites preserve polished, mirror-like slip surfaces at which grains were truncated, rather than comminuted in distributed deformation (second arrow in Figure 4), indicating a least one cycle of fault healing. Preferred parting of slip surfaces on either side of ultracataclasite layers and the reactivation of multiple slip events on one single interface, as indicated by multiple slickenline orientations that are preserved on a few slip surfaces, lead us to believe that following lithification of the ultracataclasite, slip occurred on the interface between lithified ultracataclasite and the host rock, rather than throughout the fault rock. However, there is no evidence to suggest the development of the ultracataclasites significantly impacted fault roughness because all of our measurements are consistent with the same fractal geometry. This may be because the mobile ultracataclasite filled available space in the slip zone, forming a mold of opposing sides of the fault. Therefore, in spite of apparently altering one side of that slip zone, we propose that mobilization and lithification played a minimal role in changing the bulk statistical properties of the fault surface from a geometric perspective.

Our observations also show individual grains ($\sim 10-100\mu m$) that protruded from slip surfaces were fractured during slip (Figure 4). At millimeter scales, shear fractures propagated into the wall rock to truncate, or scallop bumps on the surface (Figure 4c). We infer a similar process for field-scale irregularities along deformation band clusters or immature fault surfaces were truncated by a throughgoing shear fracture that hosted the subsequent fault slip (Figure 2c).

5.3. Scale-Invariant Wear

The single smoothing exponent appropriate to the submillimeter to centimeter length scales in our results indicate that none of the processes described above dominated the wear during slip (Brodsky et al., 2016; Kirkpatrick & Brodsky, 2014). Coherent smoothing exponents found in this study, along with Hurst exponents that are insensitive to slip (this study; Brodsky et al., 2011; Candela et al., 2012), lead us to infer that wear on faults must occur over the entire fractal bandwidth and that, likely, a single mechanism underlies its behavior. We suggest that wear occurs by fracture induced by asperity failure at all scales (consistent with Brodsky et al., 2016) rather than by gradual abrasion. In our microstructural observations, sheared tops on protruding grains illustrate asperity failure (as seen in Figures 3 and 4).

Failure during asperity collision occurs if the energy required for asperities to slip past one another exceeds the fracture energy required to propagate a fracture through either asperity (Wang & Scholz, 1994). Taller and narrower asperities, which require more energy to slip past an opposing asperity, are more prone to wear down than short and wide asperities, regardless of the length scale. We propose that this simple mechanical premise can be applied to a multiscale wear process on fractal rough interfaces that accumulate large slip and consider asperity collisions from small to large length scales.

To both illustrate and test the feasibility of a multiscale wear process, we utilized a work minimization framework within the 2-D boundary element method code GRowth by Optimization of Work (McBeck et al., 2016), which harnesses FRIC2D (Cooke & Pollard, 1997; Savage & Cooke, 2010). A detailed outline of the model outline can be found in the supporting information (Cooke & Madden, 2014; Cooke & Pollard, 1997; Crouch et al., 1982; McBeck et al., 2017, 2016; Madden et al., 2017; Newman & Griffith, 2014; Savage & Cooke, 2010). We explore the failure of individual, initially mated, sinusoidal asperities as a result of an increment of slip over a range of length scales by varying the initial asperity height as a proxy for length scale. Our goal is to gain qualitative insight into the smoothing rate as a function of initial asperity aspect ratio (height over length). We discretized the initial fault and boundary condition geometry with dislocation elements. We then prescribed displacement along the boundaries to reproduce dextral simple shear deformation. Tractions and shear offsets were then solved for along the frictional fault as well as stresses and displacements in the surrounding material. Increased stresses in the surrounding material may lead to development in new failure surfaces. Finding the failure path that optimizes work has shown success in evaluating off-fault tensile damage (Savage & Cooke, 2010) and the energy partition on rough fault systems (Newman & Griffith, 2014) and has proven to be robust in reproducing en echelon fault linkage experiments (Madden et al., 2017; McBeck et al., 2017, 2016).

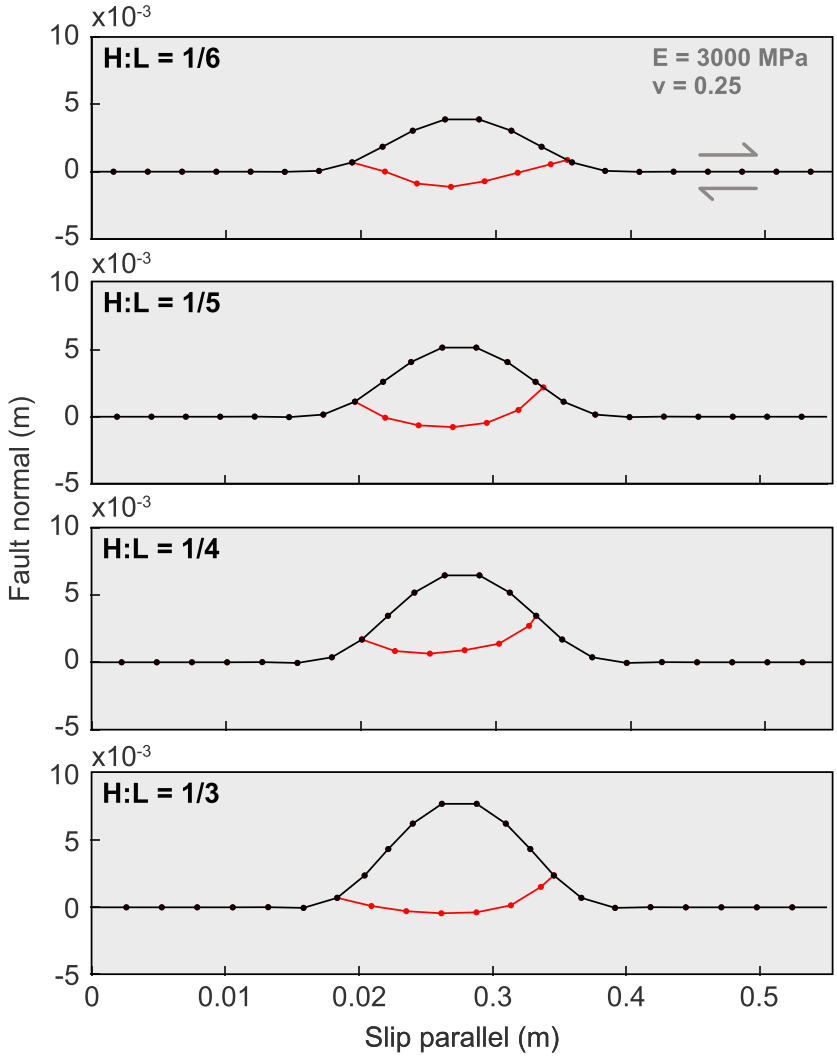

Figure 8. Two-dimensional numerical simulation of asperities of various aspect ratios failing under dextral simple shear displacement loading. The initial geometry is indicated in black with the new fracture that was grown indicated in red.

The models, shown in Figure 8, reproduce key elements of our results. Asperity failure can, as expected, occur at a range of different aspect ratios. We also produce *scalloped* asperity truncation, similar to those shown in Figures 4 and 2c, especially as the height of the initial asperity is reduced. Finally, we find that the absolute change in aspect ratio over an increment of slip decreases with initial asperity aspect ratio. These results imply that for a single asperity, the final crack geometry is sensitive to the initial asperity geometry. Specifically, the implicit relationship qualitatively reproduces the observed asymptotically decreasing wear rate with slip as faults and its population of asperities become smoother.

Because the roughness of fault surfaces is anisotropic, they have the appearance of a series of elongate ellipsoidal bumps and troughs aligned with the slip direction. When one of these ellipsoids fails, there is a single change in height associated with the removal of the asperity but that change in height is associated with different length scales in the slip-perpendicular and slip-parallel directions. Viewed in the slip-perpendicular cross section, the asperity is relatively narrow so failure occurs at a high aspect ratio, whereas in the slip-parallel cross section, the asperity is relatively long and the aspect ratio relatively small. This coupled change in asperity size, when iterated at all scales, maintains the consistent anisotropy in the slip surface roughness. Our observations suggest that averaged over the fault surface, smoothing with slip can be explained by these coupled fractional changes in the two measured orientations. Anisotropy in wear is maintained in the prefactor, A, to the empirical smoothing law (equation (2) though identifying the controls on A requires further work.

The relationship between geometrical evolution and the geometrical state that is emergent from the modeling results and required by the observations is consistent, at least qualitatively, with the overall smoothing trends we describe. The absence of a characteristic scale reconciles the evidence of wear on faults with unchanged scaling exponents and fixed geometric anisotropy. The implicit differential relationship also provides a simple mechanism by which its effectiveness decreases as fault topography smooths down.

Our models consider asperities in contact across fully mated surfaces rather than asperities that partially overlap within an area of real contact between nominally flat surfaces (Wang & Scholz, 1994). At macroscopic scales, mated contact appears to be a reasonable assumption (Chester & Chester, 2000; Kirkpatrick et al., 2018; Scholz, 1988). If surfaces are effectively mated and asperity failure governs the wear behavior with slip, we predict that factors promoting fracture, such as reduced confining stress and preexisting damage (Scholz, 2002), would favor higher wear rates. However, the normal stress dependence is opposite to traditional wear models (as in Archard, 1953; Bowden & Tabor, 2001; Greenwood & Williamson, 1966; Scholz, 1987; Wang & Scholz, 1994). At micromechanical scales, when the asperities are smaller than the dimensions of the regions of real contact across rough surfaces, increased confining stress increases both the number of contacts (Archard, 1953) and the relative overlap between asperities (Wang & Scholz, 1994). We suggest that at the macroscopic scales encompassed by our observations, which are relevant to large-scale asperity failure, the mated geometry obviates such effects. This geometrical distinction underscores that wear by asperity failure in a multiscale fractal set might be fundamentally different to traditional micromechanical wear.

6. Conclusions

We investigated the evolution of fault surfaces in normal faults cutting porous sandstones with offsets from 10^{-2} to 10^{1} m. The surfaces, which are preserved both at the edge of fault rock layers and directly truncating protolith grains, record a progression from dull, strongly striated, sinuous, and laterally discontinuous faults toward mirror-like, planar, and continuous faults. We measured the roughness of the surfaces with a range of optical profilers and found that slip surfaces (1) are systematically smoother than the joints or deformation bands from which they nucleate and (2) smooth with slip at least from the submillimeter to centimeter scale. Our data suggest that the complete geometrical and slip scaling of slip-parallel roughness is captured, to a first order, by the following:

$$P(\lambda, D) \approx 6 \times 10^{-10} \frac{\lambda^{1.8}}{D} \tag{5}$$

or equivalently,

$$RMS(L, D) \approx 3 \times 10^{-5} \frac{L^{0.4}}{D^{0.5}}. \tag{6}$$

We document a similar evolution of roughness with slip in the slip-perpendicular direction implying that the anisotropy ratio is maintained with slip. Our field and microstructural observations, roughness measurements, and numerical models indicate that this progression is enabled, not by a single-scale abrasion process but rather by a combination of wear processes, including grain plucking, scalloped fractures, and branching occurring at all scales we observed. These processes are all manifestations of asperity failure. We show that the fractal geometry of faults can be maintained during wear caused by slip when asperity failure occurs over all length scales. With our results, the extensive literature covering the geomechanical implications of roughness (e.g., Dunham et al., 2011; Fang & Dunham, 2013; Harbord et al., 2017; Marone & Cox, 1994; Zielke & Mai, 2016; Zielke et al., 2017) implies a measurable difference between earthquakes occurring on major faults and earthquakes occurring, for example, off-fault along immature fractures.

Acknowledgments
Many thanks to Laurent Maerten for providing GPS data to produce fault offset profiles in the Chimney Rock Fault Array. We also thank Emily Brodsky for thoughtful insights, Richard Chromik for providing access to the white light interferometer, and Jess McBeck for extensive assistance with the model setup. Chris Harbord and an anonymous reviewer are thanked for thorough reviews that greatly improved the manuscript. This work was funded in part through a Geological Society of America Graduate Student Research Grant. Scan data will be made available on the following repository (https://osf.io/cqdgr/) or upon request by email.

References

Antonellini, M. A., Aydin, A., & Pollard, D. D. (1994). Microstructure of deformation bands in porous sandstones at Arches National Park, Utah. *Journal of Structural Geology*, *16*(7), 941–959.

Archard, J. (1953). Contact and rubbing of flat surfaces. *Journal of Applied Physics*, *24*(8), 981–988.

Aydin, A. (1977). *Faulting in sandstone*, (PhD thesis), Stanford, CA.

Aydin, A., & Johnson, A. M. (1978). Development of faults as zones of deformation bands and as slip surfaces in sandstone. *Pure and Applied Geophysics*, *116*(4), 931–942.

Badt, N., Hatzor, Y. H., Toussaint, R., & Sagy, A. (2016). Geometrical evolution of interlocked rough slip surfaces: The role of normal stress. *Earth and Planetary Science Letters*, *443*, 153–161.

Biegel, R., Wang, W., Scholz, C., & BorrNoTr, G. (1992). 1. effects of surface roughness on initial friction and slip hardening in westerly granite. *Journal of Geophysical Research*, *97*(B6), 8951–8964.

Bistacchi, A., Griffith, W. A., Smith, S. A., Di Toro, G., Jones, R., & Nielsen, S. (2011). Fault roughness at seismogenic depths from lidar and photogrammetric analysis. *Pure and Applied Geophysics*, *168*(12), 2345–2363.
Bletery, Q., Thomas, A. M., Rempel, A. W., Karlstrom, L., Sladen, A., & De Barros, L. (2016). Mega-earthquakes rupture flat megathrusts. *Science*, *354*(6315), 1027–1031.
Bowden, F. P., & Tabor, D. (2001). *The Friction and Lubrication of Solids* (Vol. 1). New York: Oxford University Press.
Bright, A. (2006). *Deformation band fault fault core: Character evolution and influence on bulk fluid flow*, (PhD thesis), Trinity College.
Brodsky, E. E., Gilchrist, J. J., Sagy, A., & Collettini, C. (2011). Faults smooth gradually as a function of slip. *Earth and Planetary Science Letters*, *302*(1), 185–193.
Brodsky, E. E., Kirkpatrick, J. D., & Candela, T. (2016). Constraints from fault roughness on the scale-dependent strength of rocks. *Geology*, *44*(1), 19–22.
Caine, J. S., Evans, J. P., & Forster, C. B. (1996). Fault zone architecture and permeability structure. *Geology*, *24*(11), 1025–1028.
Candela, T., Renard, F., Bouchon, M., Brouste, A., Marsan, D., Schmittbuhl, J., & Voisin, C. (2009). Characterization of fault roughness at various scales: Implications of three-dimensional high resolution topography measurements. *Pure and Applied Geophysics*, *166*(10-11), 1817–1851.
Candela, T., Renard, F., Klinger, Y., Mair, K., Schmittbuhl, J., & Brodsky, E. E. (2012). Roughness of fault surfaces over nine decades of length scales. *Journal of Geophysical Research*, *117*, B08409. https://doi.org/10.1029/2011JB009041
Chester, F. M., & Chester, J. S. (2000). Stress and deformation along wavy frictional faults. *Journal of Geophysical Research*, *105*(B10), 23,421–23,430.
Chester, F., & Logan, J. (1986). Implications for mechanical properties of brittle faults from observations of the Punchbowl fault zone, California. *Pure and Applied Geophysics*, *124*(1-2), 79–106.
Cooke, M. L., & Madden, E. H. (2014). Is the Earth lazy? A review of work minimization in fault evolution. *Journal of Structural Geology*, *66*, 334–346.
Cooke, M., & Pollard, D. (1997). Bedding-plane slip in initial stages of fault-related folding. *Journal of Structural Geology*, *19*(3-4), 567–581.
Crouch, S. L., & Starfield, A. (1982). *Boundary element methods in solid mechanics: With applications in rock mechanics and geological engineering*. London: Allen & Unwin.
Davatzes, N. C. (2003). *Fault architecture as a function of deformation mechanism in clastic rocks with an emphasis on sandstone*, (PhD thesis), Stanford University, CA.
Davatzes, N. C., Aydin, A., & Eichhubl, P. (2003). Overprinting faulting mechanisms during the development of multiple fault sets in sandstone, Chimney Rock fault array, Utah, USA. *Tectonophysics*, *363*(1), 1–18.
Davidesko, G., Sagy, A., & Hatzor, Y. H. (2014). Evolution of slip surface roughness through shear. *Geophysical Research Letters*, *41*, 1492–1498. https://doi.org/10.1002/2013GL058913
Dimri, V. P. (2000). *Application of Fractals in Earth Sciences*. Rotterdam, Netherlands: CRC Press.
Doblas, M. (1998). Slickenside kinematic indicators. *Tectonophysics*, *295*(1), 187–197.
Doelling, H. H., & Willis, G. C. (2008). *Geologic map of the Smoky Mountain 30'X 60'Quadrangle, Kane and San Juan Counties, Utah and Coconino County, Arizona*. Salt Lake City, UT: Utah Geological Survey.
Dunham, E. M., Belanger, D., Cong, L., & Kozdon, J. E. (2011). Earthquake ruptures with strongly rate-weakening friction and off-fault plasticity, Part 2: Nonplanar faults. *Bulletin of the Seismological Society of America*, *101*(5), 2308–2322.
Engelder, J. T. (1974). Cataclasis and the generation of fault gouge. *Geological Society of America Bulletin*, *85*(10), 1515–1522.
Fang, Z., & Dunham, E. M. (2013). Additional shear resistance from fault roughness and stress levels on geometrically complex faults. *Journal of Geophysical Research: Solid Earth*, *118*, 3642–3654. https://doi.org/10.1002/jgrb.50262
Fossen, H., Schultz, R. A., Shipton, Z. K., & Mair, K. (2007). Deformation bands in sandstone: A review. *Journal of the Geological Society*, *164*(4), 755–769.
Fossen, H., Schultz, R. A., & Torabi, A. (2011). Conditions and implications for compaction band formation in the Navajo sandstone, Utah. *Journal of Structural Geology*, *33*(10), 1477–1490.
Greenwood, J., & Williamson, J. (1966). Contact of nominally flat surfaces. *Proceedings of the Royal Society of London A: Mathematical, Physical and Engineering Sciences* (Vol. 295, pp. 300–319). London: The Royal Society.
Hancock, P., & Barka, A. (1987). Kinematic indicators on active normal faults in western Turkey. *Journal of Structural Geology*, *9*(5-6), 573–584.
Harbord, C. W., Nielsen, S. B., De Paola, N., & Holdsworth, R. E. (2017). Earthquake nucleation on rough faults. *Geology*, *45*(10), 931–934.
Johansen, T. E. S., & Fossen, H. (2008). Internal geometry of fault damage zones in interbedded siliciclastic sediments. *Geological Society, London, Special Publications*, *299*(1), 35–56.
Jones, R., Kokkalas, S., & McCaffrey, K. (2009). Quantitative analysis and visualization of nonplanar fault surfaces using terrestrial laser scanning (lidar)—The Arkitsa fault, central Greece, as a case study. *Geosphere*, *5*(6), 465–482.
Kelley, V. C., & Clinton, N. J. (1960). *Fracture Systems and Tectonic Elements of the Colorado Plateau*. Albuquerque, New Mexico: University of New Mexico Press.
Kirkpatrick, J. D., & Brodsky, E. E. (2014). Slickenline orientations as a record of fault rock rheology. *Earth and Planetary Science Letters*, *408*, 24–34.
Kirkpatrick, J., Shervais, K., & Ronayne, M. (2018). Spatial variation in the slip zone thickness of a seismogenic fault. *Geophysical Research Letters*, *45*, 7542–7550. https://doi.org/10.1029/2018GL078767
Krantz, R. W. (1988). Multiple fault sets and three-dimensional strain: Theory and application. *Journal of Structural Geology*, *10*, 225–237.
Lay, T., Kanamori, H., & Ruff, L. (1982). The asperity model and the nature of large subduction zone earthquakes. *Earthquake Prediction Research*, *1*(1), 3–71.
Lee, J.-J., & Bruhn, R. L. (1996). Structural anisotropy of normal fault surfaces. *Journal of Structural Geology*, *18*(8), 1043–1059.
Ludington, S., Moring, B. C., Miller, R. J., Stone, P. A., Bookstrom, A. A., Bedford, D. R., et al. (2007). Preliminary integrated geologic map databases for the United States. Western States: California, Nevada, Arizona, Washington, Oregon, Idaho, and Utah.
Madden, E. H., Cooke, M. L., & McBeck, J. (2017). Energy budget and propagation of faults via shearing and opening using work optimization. *Journal of Geophysical Research: Solid Earth*, *122*, 6757–6772. https://doi.org/10.1002/2017JB014237
Maerten, L., Pollard, D. D., & Maerten, F. (2001). Digital mapping of three-dimensional structures of the chimney rock fault system, central Utah. *Journal of Structural Geology*, *23*(4), 585–592.
Mandelbrot, B. B. (1985). Self-affine fractals and fractal dimension. *Physica Scripta*, *32*(4), 257.
Mandelbrot, B. B., Passoja, D. E., & Paullay, A. J. (1984). Fractal character of fracture surfaces of metals. *Nature*, *308*, 721–722.
Marone, C., & Cox, S. (1994). Scaling of rock friction constitutive parameters: The effects of surface roughness and cumulative offset on friction of gabbro. *Pure and Applied Geophysics*, *143*(1), 359–385.

McBeck, J. A., Cooke, M. L., Herbert, J. W., Maillot, B., & Souloumiac, P. (2017). Work optimization predicts accretionary faulting: An integration of physical and numerical experiments. *Journal of Geophysical Research: Solid Earth*, *122*, 7485–7505. https://doi.org/10.1002/2017JB013931

McBeck, J. A., Madden, E. H., & Cooke, M. L. (2016). Growth by optimization of work (grow): A new modeling tool that predicts fault growth through work minimization. *Computers & Geosciences*, *88*, 142–151.

Means, W. (1987). A newly recognized type of slickenside striation. *Journal of Structural geology*, *9*(5-6), 585–590.

Myers, R. D. (1999). *Structure and hydraulics of brittle faults in sandstone,* (PhD thesis), Stanford University, CA.

Newman, P. J., & Griffith, W. A. (2014). The work budget of rough faults. *Tectonophysics*, *636*, 100–110.

Ohnaka, M. (2013). *The Physics of Rock Failure and Earthquakes*. Cambridge: Cambridge University Press.

Ohnaka, M., & Shen, L.-f. (1999). Scaling of the shear rupture process from nucleation to dynamic propagation: Implications of geometric irregularity of the rupturing surfaces. *Journal of Geophysical Research*, *104*(B1), 817–844.

Okubo, P. G., & Dieterich, J. H. (1984). Effects of physical fault properties on frictional instabilities produced on simulated faults. *Journal of Geophysical Research*, *89*(B7), 5817–5827.

Otsuki, K., Monzawa, N., & Nagase, T. (2003). Fluidization and melting of fault gouge during seismic slip: Identification in the Nojima fault zone and implications for focal earthquake mechanisms. *Journal of Geophysical Research*, *108*(B4), 2192. https://doi.org/10.1029/2001JB001711

Palmer, A. C., & Rice, J. (1973). The growth of slip surfaces in the progressive failure of over-consolidated clay. In *Proceedings of the royal society of London A: Mathematical, physical and engineering sciences* (Vol. 332, pp. 527–548). Great Britain: The Royal Society.

Petit, J. (1987). Criteria for the sense of movement on fault surfaces in brittle rocks. *Journal of Structural Geology*, *9*(5-6), 597–608.

Power, W. L., & Tullis, T. E. (1991). Euclidean and fractal models for the description of rock surface roughness. *Journal of Geophysical Research*, *96*(B1), 415–424.

Power, W., Tullis, T., Brown, S., Boitnott, G., & Scholz, C. (1987). Roughness of natural fault surfaces. *Geophysical Research Letters*, *14*(1), 29–32.

Power, W. L., Tullis, T. E., & Weeks, J. D. (1988). Roughness and wear during brittle faulting. *Journal of Geophysical Research*, *93*(B12), 15,268–15,278.

Renard, F., Candela, T., & Bouchaud, E. (2013). Constant dimensionality of fault roughness from the scale of micro-fractures to the scale of continents. *Geophysical Research Letters*, *40*, 83–87. https://doi.org/10.1029/2012GL054143

Renard, F., Voisin, C., Marsan, D., & Schmittbuhl, J. (2006). High resolution 3D laser scanner measurements of a strike-slip fault quantify its morphological anisotropy at all scales. *Geophysical Research Letters*, *33*, L04305. https://doi.org/10.1029/2005GL025038

Robertson, E. C. (1982). Continuous formation of gouge and breccia during fault displacement. In *The 23Rd US Symposium on Rock Mechanics USRMS* (pp. 25–27). August, Berkeley, CA: American Rock Mechanics Association.

Sagy, A., & Brodsky, E. E. (2009). Geometric and rheological asperities in an exposed fault zone. *Journal of Geophysical Research*, *114*, B02301. https://doi.org/10.1029/2008JB005701

Sagy, A., Brodsky, E. E., & Axen, G. J. (2007). Evolution of fault-surface roughness with slip. *Geology*, *35*(3), 283–286.

Savage, H. M., & Cooke, M. L. (2010). Unlocking the effects of friction on fault damage zones. *Journal of Structural Geology*, *32*(11), 1732–1741.

Schmittbuhl, J., Gentier, S., & Roux, S. (1993). Field measurements of the roughness of fault surfaces. *Geophysical Research Letters*, *20*(8), 639–641.

Schmittbuhl, J., Vilotte, J.-P., & Roux, S. (1995). Reliability of self-affine measurements. *Physical Review E*, *51*(1), 131.

Scholz, C. H. (1987). Wear and gouge formation in brittle faulting. *Geology*, *15*(6), 493–495.

Scholz, C. (1988). The critical slip distance for seismic faulting. *Nature*, *336*(6201), 761.

Scholz, C. H. (2002). *The Mechanics of Earthquakes and Faulting*. New York: Cambridge University Press.

Scholz, C. H., & Aviles, C. (1986). The fractal geometry of faults and faulting. In S. Das, J. Boatwright, & C. H. Scholz (Eds.), *Earthquake Source Mechanics* (pp. 147–155). Washington, DC: American Geophysical Union.

Shervais, K. A., & Kirkpatrick, J. D. (2016). Smoothing and re-roughening processes: The geometric evolution of a single fault zone. *Journal of Structural Geology*, *91*, 130–143.

Shipton, Z. K. (1999). *Fault displacement profiles and off-fault deformation: Interpreting the record of fault growth at the chimney rock fault array, Utah USA*, (PhD thesis), University of Edinburgh.

Shipton, Z., & Cowie, P. (2001). Damage zone and slip-surface evolution over μm to km scales in high-porosity Navajo sandstone, Utah. *Journal of Structural Geology*, *23*(12), 1825–1844.

Shipton, Z. K., & Cowie, P. A. (2003). A conceptual model for the origin of fault damage zone structures in high-porosity sandstone. *Journal of Structural Geology*, *25*(3), 333–344.

Shipton, Z. K., Evans, J. P., Robeson, K. R., Forster, C. B., & Snelgrove, S. (2002). Structural heterogeneity and permeability in faulted eolian sandstone: Implications for subsurface modeling of faults. *AAPG Bulletin*, *86*(5), 863–883.

Shipton, Z., Evans, J., & Thompson, L. (2005). The geometry and thickness of deformation-band fault core and its influence on sealing characteristics of deformation-band fault zones. In R. Sorkhabi & Y. Tsuji (Eds.), *Faults, Fluid Flow, and Petroleum Traps* (pp. 181–195). Tulsa, OK: American Association of Petroleum Geologists.

Shipton, Z. K., Soden, A. M., Kirkpatrick, J. D., Bright, A. M., & Lunn, R. J. (2006). How thick is a fault? Fault displacement-thickness scaling revisited. In R. Abercrombie, A. McGarr, G. Di Toro, & H. Kanamori (Eds.), *Earthquakes: Radiated Energy and the Physics of Faulting* (pp. 193–198). Washington, DC: American Geophysical Union.

Sibson, R. (1977). Fault rocks and fault mechanisms. *Journal of the Geological Society*, *133*(3), 191–213.

Sibson, R. H. (2003). Thickness of the seismic slip zone. *Bulletin of the Seismological Society of America*, *93*(3), 1169–1178.

Swanson, M. T. (1989). Sidewall ripouts in strike-slip faults. *Journal of Structural Geology*, *11*(8), 933–948.

Trauth, M. H., Gebbers, R., Marwan, N., & Sillmann, E. (2007). *MATLAB Recipes for Earth Sciences* (Vol. 34). New York: Springer.

Vrolijk, P., Myers, R., Sweet, M. L., Shipton, Z. K., Dockrill, B., Evans, J. P., et al. (2005). Anatomy of reservoir-scale normal faults in central Utah: Stratigraphic controls and implications for fault zone evolution and fluid flow. *Field Guides*, *6*, 261–282.

Wang, W., & Scholz, C. H. (1994). Wear processes during frictional sliding of rock: A theoretical and experimental study. *Journal of Geophysical Research*, *99*, 6789–6789.

Zielke, O., Galis, M., & Mai, P. (2017). Fault roughness and strength heterogeneity control earthquake size and stress drop. *Geophysical Research Letters*, *44*, 777–783. https://doi.org/10.1002/2016GL071700

Zielke, O., & Mai, P. M. (2016). Sub-patch roughness in earthquake rupture investigations. *Geophysical Research Letters*, *43*, 1893–1900. https://doi.org/10.1002/2015GL067084